metals

MDPI

Article

Experimental and Molecular Dynamics-Based Study on the Influence Mechanism of a Lead–Bismuth Eutectic Corrosive Environment on the Thermal Conductivity of T91 Steel

Xinxin Gao [1], Xian Zeng [2,*] and Zhaoxuan Sun [2]

[1] School of Nuclear Science and Technology, University of Science and Technology of China, Hefei 230026, China; gao_xinx@163.com
[2] Advanced Nuclear Energy Operations Research Institute, China Nuclear Power Technology Research Institute Co., Ltd., Shenzhen 518031, China; 18126359539@163.com
* Correspondence: zeng.xian12@163.com

Abstract

Under lead–bismuth eutectic (LBE) corrosion conditions, the multilayer oxide layer that forms on T91 steel adversely affects on its thermal conductivity. This study systematically conducted corrosion experiments under varying temperatures, durations, oxygen concentrations, and bismuth (Bi) content. By combining microstructural characterization with laser flash measurements of thermal conductivity, the evolution of T91 thermal conductivity under different corrosion conditions was revealed. Based on these findings, molecular dynamics simulations based on the neuroevolution potential (NEP) framework were employed to construct a T91/Fe-Cr spinel/Fe_3O_4 multilayer heterojunction model, enabling precise determination of the intrinsic thermal resistances at the two interfaces. By coupling the interfacial thermal resistances with experimental data, the macroscopic effective thermal conductivities of Fe-Cr spinel and Fe_3O_4 in real corrosion environments were calculated to be 1.68 W/(m·K) and 2.19 W/(m·K), respectively. These values are significantly lower than those reported for pure phases, thus revealing the inhibitory effect of defects and pores in actual oxide layers on heat transport. This research establishes a multiscale analytical method spanning from atomic-scale interfacial thermal resistance to macroscopic heat transfer properties of oxide layers, thereby providing a theoretical basis and data support for the thermal performance evaluation and service life prediction of LFR structural materials.

Keywords: T91 ferritic/martensitic steel; lead–bismuth eutectic (LBE) corrosion; oxide layer thermal conductivity; molecular dynamics simulation; neuroevolution potential (NEP); interfacial thermal resistance

Check for updates

Academic Editor: Sanichiro Yoshida

Received: 11 May 2026
Revised: 17 June 2026
Accepted: 24 June 2026
Published: 26 June 2026

Copyright: © 2026 by the authors. Licensee MDPI, Basel, Switzerland. This article is an open access article distributed under the terms and conditions of the Creative Commons Attribution (CC BY) license.

1. Introduction

The lead-cooled fast reactor (LFR) is a promising fourth-generation nuclear system with good inherent safety, high fuel efficiency, and the ability to transmute its waste. Passive safety features, such as reactor vessel cooling systems, further enhance its accident tolerance and potential for commercialization [1,2].

Among current candidate structural materials for LFR systems, T91 ferritic/martensitic steel is particularly notable for its potential uses in core heat transfer tubes, fuel cladding, and heat exchangers owing to its high-temperature strength (yield strength $\geq$ 300 MPa at 600 °C), excellent creep resistance, and good oxidation resistance in oxygen-controlled

lead–bismuth eutectic (LBE) environments, achieved through the formation of a protective Cr-rich oxide scale [3,4].

Current engineering design targets require a corrosion rate below 0.1 mm/year in LBE at 400–550 °C and a defect-free oxide layer [5]. From the standpoint of long-term service reliability, the thermal conductivity of candidate structural materials must remain sufficiently stable throughout the reactor design lifetime, typically on the order of 40–60 years. This requirement is particularly important for LFRs, whose core design is governed by relatively stringent thermal margins and strong coupling among neutronic, thermal–hydraulic, thermo-mechanical, and safety constraints. A pronounced degradation in thermal conductivity during long-term exposure would impair heat transfer across the liquid–solid interface, increase the interfacial temperature gradient, and promote local heat accumulation in the core and heat-transfer components. This, in turn, may elevate thermal stress, reduce structural margins, and increase the susceptibility of critical components to thermally induced damage. For this reason, controlling the reduction in thermal conductivity within an acceptable range, for example, below approximately 25% over the service period, is an important material performance target for maintaining heat-exchange efficiency and preventing thermal stress failure in LFR systems [6–9].

However, when exposed to liquid LBE under oxygen-controlled conditions, T91 does not remain a bare metallic surface; instead, it typically develops a duplex oxide scale mainly composed of an inner Fe-Cr spinel layer adjacent to the steel substrate and an outer magnetite (Fe_3O_4) layer in contact with the liquid metal. This characteristic oxide architecture has been widely reported for Fe–9Cr–1Mo martensitic steels in LBE environments over the relevant reactor temperature range and is generally regarded as the typical oxidation response of T91 in oxygen-containing lead-based environments [10–12]. Existing studies further indicate that the growth of this duplex scale follows diffusion-controlled behavior, with the outer magnetite layer primarily associated with outward iron transport, whereas the inner Fe-Cr spinel layer forms at the metal/oxide interface and is closely related to oxygen transport toward the substrate [13]. From an engineering perspective, the formation of such an oxide film is of central importance because it retards direct dissolution attack by the liquid metal and thereby contributes to the corrosion tolerance of T91. However, the intrinsic thermal conductivity of such oxide layers is significantly lower than that of the matrix [14]. Further, the thermal conductivities of Fe-Cr spinel and Fe_3O_4 oxide layers are typically based on pure-phase materials, and there are no actual thermal conductivity values derived from corrosion experiments in LFRs. In addition, the thickness, phase composition, and microstructure dynamically evolve with factors such as corrosion time, temperature, oxygen concentration, and bismuth (Bi) content, leading to a nonlinear deterioration in the material's overall thermal conductivity [15–17]. This, in turn, alters the thermal–hydraulic characteristics of the system and places high demands on the precision of engineering design [5].

To address these limitations, this study establishes a multi-scale integrated framework comprising "corrosion testing–microscopic characterization–molecular dynamics simulation–macroscopic thermal resistance calculation and measurement." The innovations of this work primarily include the following three aspects: (1) The neuroevolution potential (NEP) model is applied to thermal transport simulations of the T91/Fe-Cr spinel/Fe_3O_4 multiphase system under lead–bismuth corrosion conditions. NEP autonomously learns energies and forces from density functional theory (DFT) calculations via neural network descriptors, combining first-principles accuracy with GPU-parallel processing efficiency. It can uniformly describe metallic bonds (T91), ionic bonds (oxides), and mixed bonding at interfaces, thereby avoiding the piecewise discontinuity errors associated with traditional potential functions. To our knowledge, few studies have applied NEP to the calculation

of interfacial thermal resistance in lead–bismuth corrosion systems. (2) Atomic-scale interfacial thermal resistance is directly coupled with macroscopic thermal conductivity measurements. Unlike previous studies that treated molecular dynamics-calculated interfacial thermal resistance as an independent output, this study simultaneously analyzes the thermal conductivity, layer thickness, and molecular dynamics-calculated interfacial thermal resistance of two sets of experimental samples with different oxide layer thicknesses. Based on a series thermal resistance model, the effective thermal conductivity of Fe_3O_4 and Fe-Cr spinel in real corrosion environments is derived. This coupling approach facilitates the establishment of a traceable closed-loop relationship between "atomic-scale interfacial thermal resistance" and "macroscopic thermal conductivity of the oxide layer." (3) The influence of corrosion temperature, time, and Bi content on the material's overall thermal conductivity is systematically investigated. By integrating results from microstructural characterization of the oxide layer, a synergistic "microstructure–thermal conductivity" analysis is conducted to clarify how the phase composition, thickness, and defects of the oxide layer modulate heat transport processes, thereby revealing the mechanisms underlying the deterioration of thermal conductivity in heat-resistant steel under LBE corrosion conditions from an experimental perspective. This provides a reference for the engineering evaluation of thermal performance in structural materials for LFRs.

2. Experimental Methods

2.1. Experimental Materials

The T91 heat-resistant steel specimens used in the experiment were processed from the same batch of raw material, and their chemical composition was determined using inductively coupled plasma mass spectrometry (Agilent 7800 ICP-MS, Agilent Technologies, Santa Clara, CA, USA), as shown in Table 1. An electric discharge wire-cutting machine was used to machine the raw material into square specimens measuring 10 mm × 10 mm × 2 mm. The specimen surfaces were ground in stages, starting with 220-grit sandpaper and progressively refining to 2000-grit sandpaper to reduce surface roughness. Subsequently, the specimen surfaces were finely polished using a diamond polishing compound until no visible scratches remained and a uniform, bright, mirror-like finish was achieved. Finally, the specimens were ultrasonically cleaned with anhydrous ethanol to remove impurities and debris generated during grinding and polishing, then dried and set aside for subsequent use.

Table 1. T91 Composition (wt.%).

Steel	Cr	W	Ni	Mn	V	Nb	Mo	Ti
T91	8.99	0.01	0.11	0.38	0.21	0.06	0.89	0.003
Steel	Al	Cu	C	N	P	S	Si	Fe
T91	0.01	0.06	0.1025	0.044	0.021	0.0004	0.22	Bal.

Figure 1 presents the microstructure of T91 heat-resistant steel at a magnification of 100×. The matrix is composed of uniformly refined tempered martensite laths that are interwoven throughout the microstructure. Numerous fine carbide particles are uniformly dispersed along the martensite lath boundaries and within the lath interiors. No abnormal microstructural constituents, such as coarse carbides, massive ferrite, or bainite, are observed within the field of view. The overall microstructure is homogeneous and compact, exhibiting a typical and well-developed tempered martensitic structure.

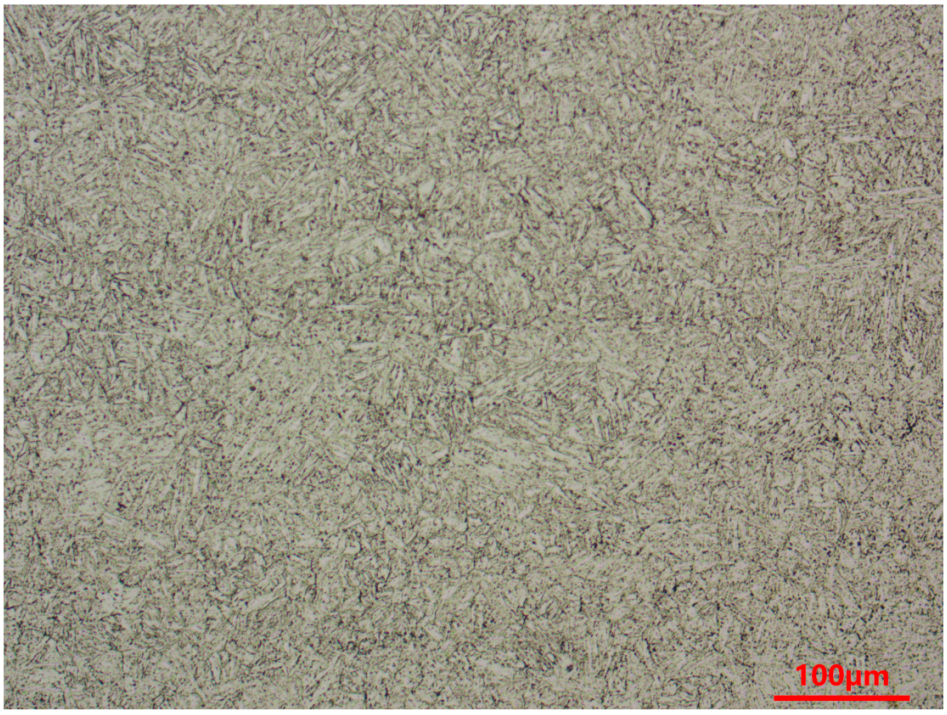

Figure 1. Tempered martensitic microstructure of T91 steel (100×).

2.2. Experimental Procedure

This experimental design covers different temperatures (400–600 °C), corrosion durations (1000 h–9000 h), oxygen concentrations (saturated oxygen, 1×10^{-6} wt.%), and Bi contents (50 wt.%, 53 wt.%, 55.5 wt.%, 60 wt.%). The aim is to investigate the effects of various corrosion variables on the structure of the T91 oxide layer and its thermal conductivity.

The apparatus for the LBE alloy corrosion experiment is shown in Figure 2. Its core components include an oxygen sensor, a temperature-measuring thermocouple, inlet and outlet gas pipes, the experimental vessel, and an automatic oxygen control system, which can precisely regulate the temperature and oxygen concentration during the corrosion process. The experimental vessel (Figure 2b) was fabricated from 316L stainless steel. To minimize corrosion by the liquid lead–bismuth alloy and ensure the reliability of the experimental results, an alumina crucible was installed inside the vessel as a protective liner.

This study employs an LSCF ($La_{1-x}Sr_xCo_{1-c}Fe_cO_{3-\delta}$, lanthanum–strontium–cobalt ferrite)/air reference oxygen sensor to conduct real-time online monitoring of oxygen concentration in lead–bismuth eutectic alloy coolant and utilizes a Proportional–Integral–Derivative closed-loop control algorithm to achieve precise regulation of oxygen concentration within the LBE system. This commercial high-precision oxygen sensor was fully calibrated using standard oxygen partial-pressure samples prior to all corrosion experiments. The intrinsic measurement precision of the sensor is within 1%, ensuring accurate quantification even at the ultra-low oxygen concentration of 1×10^{-6} wt.%. Prior to the experiment, target oxygen concentration values and upper and lower control thresholds are preset. When the monitored oxygen concentration exceeds the upper threshold, the control system automatically closes the air branch control valve and simultaneously opens the hydrogen branch control valve; continuous hydrogen injection effectively curbs the increase in oxygen concentration, causing it to transition into a sustained decline. When the oxygen concentration decreases below the preset lower threshold, the system automatically closes the hydrogen branch control valve and reopens the air branch control valve; the

introduction of air reverses the downward trend of oxygen concentration, causing it to gradually increase and exhibit a sustained upward trajectory. Different corrosion experiments at varying oxygen concentrations employ distinct control methods: In the saturated oxygen concentration experiment, a fixed flow rate of Ar + air mixture is continuously introduced into the tank until the oxygen concentration in the lead–bismuth reaches saturation and remains stable throughout the process; in the 1×10^{-6} wt.% oxygen concentration test, the gaseous automatic oxygen control system dynamically adjusts the injection flow rates of the Ar + air and Ar+5% H_2 mixtures to precisely stabilize the oxygen concentration in the lead–bismuth alloy at the target value.

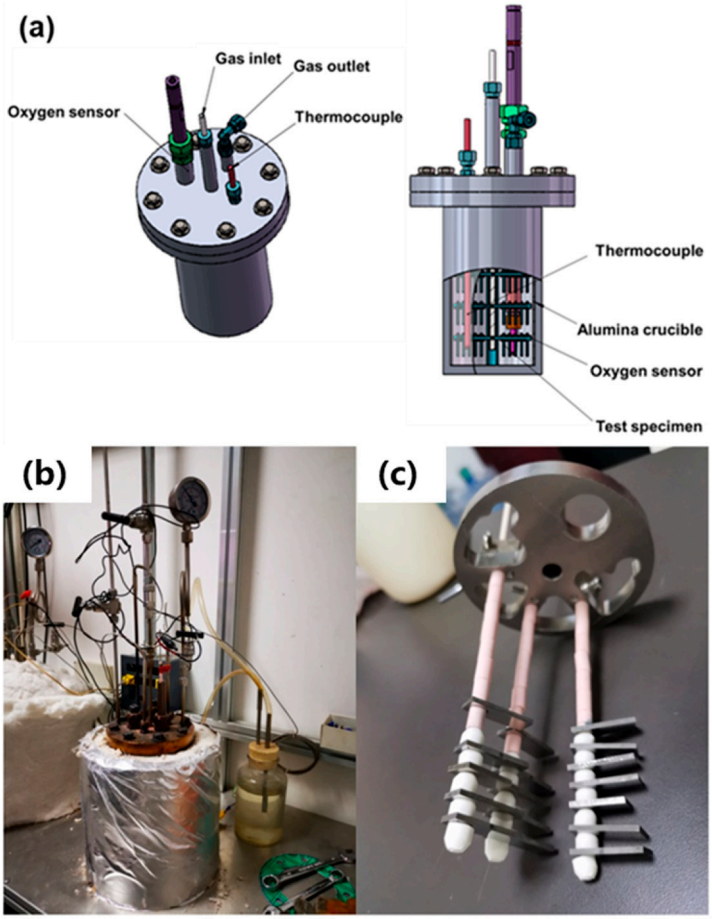

Figure 2. Schematic diagram and photograph of the static lead–bismuth alloy corrosion test apparatus: (**a**) Schematic diagram; (**b**) Photograph; (**c**) Sample suspension device.

Two oxygen conditions, namely saturated and 1×10^{-6} wt.% oxygen, were employed for the corrosion tests in this study. The selection of these oxygen levels was based on the fundamental oxidation mechanisms and the practical engineering requirements of lead–bismuth-cooled reactors, respectively.

Saturated oxygen corresponds to the maximum solubility limit of oxygen in liquid lead or lead–bismuth eutectic (LBE) at the test temperature and represents the optimal condition for the formation of protective oxide scales. Under saturated oxygen conditions, the chemical potential gradient driving steel oxidation reaches its maximum value, providing the greatest thermodynamic driving force for oxidation. This environment promotes the rapid formation of continuous, dense, and well-adherent passivating oxide films on the alloy substrate within a practical experimental duration, thereby enabling comprehensive characterization of the microstructural evolution of fully developed oxide layers.

An oxygen concentration of 1×10^{-6} wt.% was selected to represent the actual operating conditions of lead–bismuth-cooled reactors. This oxygen level satisfies two critical operational requirements simultaneously. It provides sufficient dissolved oxygen to facilitate the spontaneous self-repair of passivating oxide scales following minor damage while preventing excessive oxidation of the liquid-metal coolant. Excessive oxidation may generate substantial oxide debris and increase the risk of flow-channel blockage within the cooling circuit. Therefore, corrosion tests conducted at an oxygen concentration of 1×10^{-6} wt.% can effectively reproduce the long-term corrosion and oxidation behavior of structural steels under realistic reactor service conditions.

The specific experimental procedure is as follows: First, a block of solid LBE alloy is placed into an alumina crucible inside the vessel and heated to 200 °C until it is completely melted; then, the sample holder, with the specimens securely fixed, is positioned directly above the vessel; the height of the ceramic rod is precisely adjusted to ensure that all of the specimens arranged in series are fully immersed in the molten LBE; after closing the vessel lid and tightening the bolts to ensure a proper seal, heating is continued to 600 °C and the temperature is maintained, after which the corrosion test timer is started.

2.3. Characterization and Analysis Methods

Corroded specimens were cut into two sections using electric discharge wire cutting. A 10 mm × 10 mm × 2 mm thin section was used for thermal conductivity measurements, and a 2 mm × 10 mm × 2 mm specimen was used for cross-sectional morphological observation of the corrosion-induced oxide layers. The sample preparation and characterization workflow is shown in Figure 3.

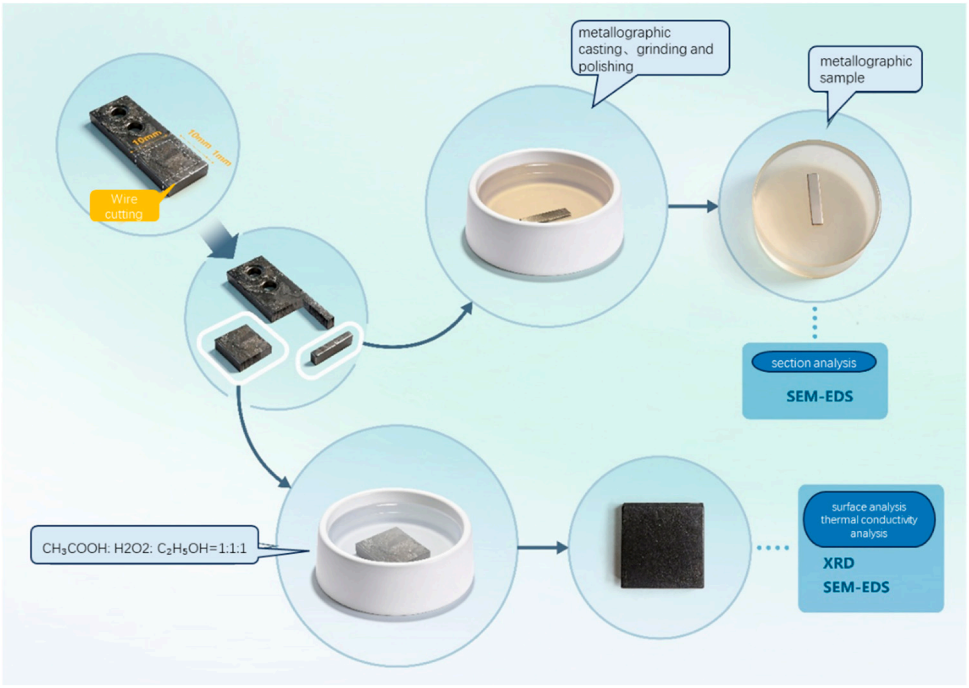

Figure 3. Sample preparation and characterization workflow.(The arrows represent the flow direction to the next step, and the dashed lines denote samples used for the corresponding experiment).

For samples used in surface phase and morphology characterization, as well as thermal conductivity measurements, residual liquid LBE alloy adhering to the surface was first removed. LBE removal was performed using a chemical cleaning method, using a cleaning solution prepared from a 1:1:1 volume ratio mixture of ethanol, hydrogen peroxide, and acetic acid. After surface pretreatment, the phase structure of the corrosion layer was

analyzed using an X-ray diffractometer (D8 Advance, Bruker AXS SE, Karlsruhe, Germany). By analyzing the XRD patterns and comparing them with Joint Committee on Powder Diffraction Standards (JCPDS) standard cards, the crystal structure and primary phase composition of the corrosion oxide layer were determined. Specimens for cross-sectional analysis were prepared using the cold mounting method. Scanning electron microscopes (GeminiSEM 500, Carl Zeiss Microscopy GmbH, Oberkochen, Germany) were used to characterize the cross-sectional corrosion morphology of the specimens. The thickness of the oxide layer was measured using secondary electron imaging. Three locations where the oxide layer covered a relatively large area were selected for measurement. The vertical distance from the substrate/oxide interface to the oxide/lead–bismuth interface was measured, and the average value was taken as the total thickness of the oxide layer for that sample. For double-layer or multi-layer structures, the thicknesses of the Fe_3O_4 layer, the Fe-Cr spinel layer, and the IOZ layer were measured separately. The chemical composition of the corrosion products was systematically characterized with the aid of the energy dispersive X-ray spectrometer (Ultim Max 65 EDS detector, Oxford Instruments, Abingdon, UK) integrated with the SEM. Typical micro-regions of the corrosion layer cross-section were selected for spot analysis, line scanning, and area scanning tests.

The thermal conductivity of the specimens was measured using a Laser flash thermal conductivity analyzer LFA457, Netzsch GmbH, Selb, Germany. The specimen surfaces were pretreated by carbon spraying prior to testing in order to reduce laser reflectivity and improve energy absorption efficiency.

2.4. Molecular Dynamics Simulation Method

Molecular dynamics (MD) is a core tool for revealing the microscopic mechanisms of thermal transport in materials at the atomic scale and has been widely applied in the study of thermal properties in complex systems. This study focuses on the T91/Fe-Cr spinel/Fe_3O_4 three-layer, multiphase, multi-element system (containing elements such as Fe, Cr, and O, with coexisting body-centered cubic (BCC)-structured metallic T91 and spinel-structured oxide phases, featuring two types of interfaces, namely, metal/oxide and oxide/oxide, as well as an Fe/Cr composition gradient). Traditional empirical potential functions (such as the metal embedded atom method and the oxide Buckingham potential) are limited to a single phase or bonding type, making it difficult to uniformly describe the complex interactions between metallic and ionic bonds across interfaces. Further, piecewise potential functions face challenges in maintaining interfacial continuity and fail to meet the accuracy requirements for simulation.

Machine learning potentials combine the high precision of DFT with the high efficiency of MD by fitting the energy and force data of atomic clusters calculated via DFT, thereby providing a solution for simulating multiphase, multi-element systems. To address the low computational efficiency of early machine learning potentials (such as the GAP potential), the NEP developed by Fan et al. utilizes a GPU-accelerated parallel architecture, achieving a computational speed nearly three orders of magnitude faster than traditional machine learning potentials. Further, after optimization, it demonstrates excellent accuracy and applicability in simulating thermal properties.

This study employs an MD simulation method based on the NEP to describe interatomic interactions within the system. Its advantages include: (1) autonomous learning of interaction patterns among different elements in metallic, oxide, and interfacial environments through a descriptor–neural network architecture, enabling a unified description of multiphase, multi-element systems; (2) accurate reproduction of the system's energy and force characteristics based on a DFT training set comprising single-phase bulk, surface, and interfacial configurations; (3) GPU parallel computing, ensuring nanosecond-scale

evolution of models with tens of thousands of atoms, meeting the efficiency requirements of non-equilibrium molecular dynamics (NEMD) simulations; and (4) accurate prediction of forces, energy, and virial stresses, providing critical inputs for heat flux and temperature distribution calculations.

Using this method, this study systematically obtained interfacial thermal resistance data for the T91/Fe-Cr spinel/Fe_3O_4 three-layer structure.

3. Molecular Dynamics-Based Study of Interfacial Thermal Resistance in Oxide Layers

In this study, a non-equilibrium MD approach was used to construct two sets of T91 bilayer oxide models in order to systematically investigate the intrinsic thermal resistances of the T91/Fe-Cr spinel and Fe-Cr spinel/Fe_3O_4 interfaces. First, atomically smooth interface models were constructed, and NEMD simulations were performed to calculate the interface temperature step and heat flux density, thereby obtaining the interfacial thermal resistance values. The calculated interfacial thermal resistance serves as an input parameter for the series thermal resistance model calculations of macroscopic thermal conductivity in multilayer materials, thereby establishing a method for predicting the heat transfer performance of oxide layers from the atomic to the macroscopic scale.

3.1. Model Development and Validation

3.1.1. Construction of Single-Component Models

Based on JCPDS standard data sheets, single-phase models for T91, Fe-Cr spinel, and Fe_3O_4 were constructed. The core parameters are as follows:

1. Fe_3O_4: Inverse spinel structure, cubic crystal system (space group Fd-3m, No. 227), with tetrahedral sites occupied by Fe^{3+} and octahedral sites occupied by a mixture of Fe^{2+} and Fe^{3+}, matching the lattice characteristics of the experimental phase (Figure 4).
2. Fe-Cr spinel: $FeCr_2O_4$ with a normal spinel structure, cubic system (space group Fd-3m), with tetrahedral sites occupied by Fe^{2+} and octahedral sites occupied by a mixture of Fe^{2+} and Fe^{3+}, consistent with the Fe/Cr ratio characterized earlier (Figure 4).
3. T91: Using BCC α-Fe as the host structure (with lattice parameters consistent with standard values), Fe atoms were randomly substituted with Fe-9Cr-1Mo-V-Nb (wt.%) components. The resulting structure was then relaxed under the NEP using an isothermal–isobaric ensemble (constant number–pressure–temperature ensemble, NPT, 0 Pa, 450 °C) to eliminate local stresses and reach an equilibrium configuration (Figure 5).

3.1.2. Validation of Single-Phase Models

To ensure the accuracy of subsequent ternary heterojunction simulations, melting point simulations and isotropic displacement analyses were performed on the constructed T91, Fe-Cr spinel, and Fe_3O_4 single-phase models to verify the structural stability of the models and the accuracy of the NEP function.

Melting point simulation: The heating–melting method was employed (NPT ensemble, 0 Pa, heating rate of 1 K/ps, 300 K–3000 K) to record the potential energy–temperature curve. When the crystal melts, atoms transition from an ordered lattice arrangement to a disordered liquid state, causing a distinct jump in the system's potential energy. On the temperature–potential or temperature–lattice size curves, the temperature corresponding to this jump is defined as the simulated melting point. As shown in Figure 6, the deviations between the simulated melting points of T91, Fe-Cr spinel, and Fe_3O_4 and their experimen-

tal values are all <10%, confirming that the NEP can accurately describe high-temperature thermodynamic behavior.

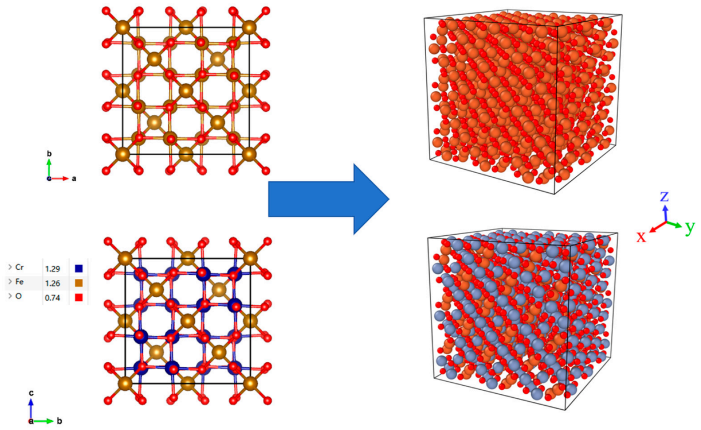

Figure 4. Two crystal structures (from the initial structure to a wide-cell single phase): Fe_3O_4 is on the top and Fe-Cr spinel is on the bottom.(Arrows mark the shift from 2D planar perspective to 3D stereoscopic perspective).

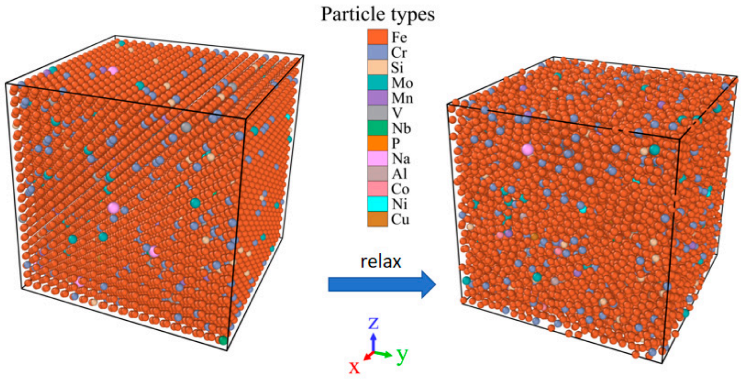

Figure 5. Configuration acquisition of T91.

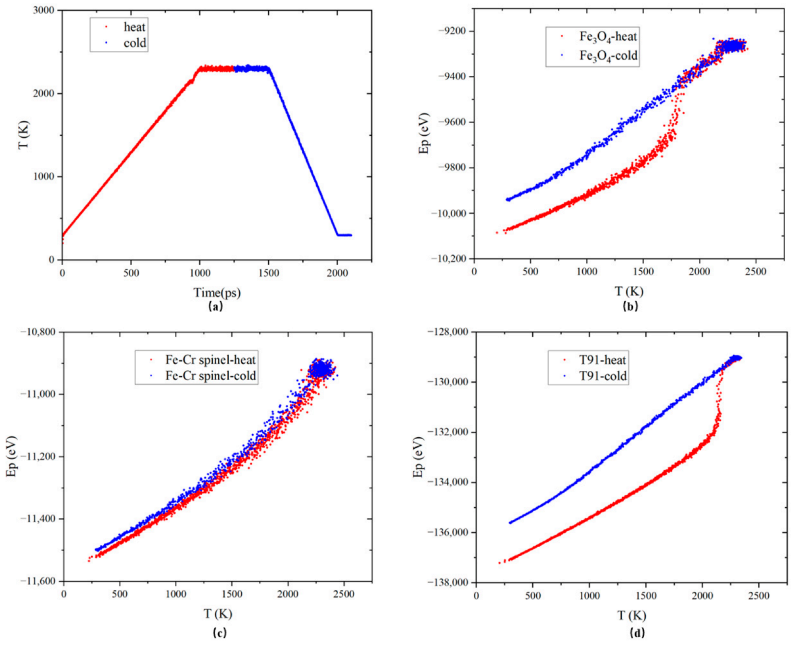

Figure 6. Heating and cooling test results: (**a**) Temperature control curve; (**b**–**d**) Potential energy curves for Fe_3O_4, Fe-Cr spinel, and T91, respectively.

Root-mean-square displacement (RMSD) analysis: Figure 7 shows that according to equilibrium MD simulations, the atomic RMSD of the three materials exhibits no significant fluctuations prior to phase transformation. After high-temperature quenching, the values still converge to stable values, with atoms vibrating only around their equilibrium positions. There is no directional diffusion or structural disorder, indicating that the single-phase models contain no initial defects and can serve as a reliable foundation for modeling heterogeneous structures.

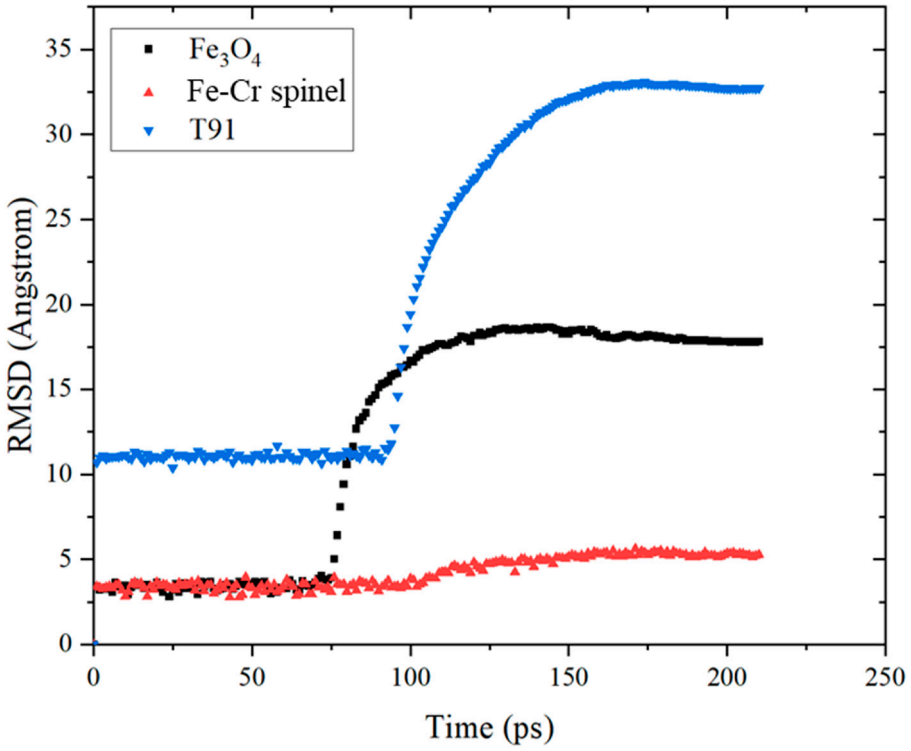

Figure 7. RMSD curves of the mean square displacement for the three-phase structure during heating and cooling tests.

In particular, the RMSD of Fe-Cr spinel exhibits negligible variation following high-temperature quenching. Owing to its dense crystal structure and excellent thermodynamic stability, the atoms remain confined to their lattice positions and undergo only small-amplitude thermal vibrations. No significant atomic diffusion or structural transformation is observed during the simulation process.

3.1.3. Construction of a Gradient-Thickness Model for Ternary Heterostructures

To investigate the effect of oxide layer thickness on interfacial heat transport, two sets of T91/Fe-Cr spinel/Fe_3O_4 heterojunction models with varying layer thicknesses were constructed along the *Y*-axis (Table 2), adhering to the principle of single-variable control:

- The T91 layer thickness was fixed at 10 nm to eliminate interference from the bulk thermal resistance of the matrix; the thicknesses of the Fe-Cr spinel layer (4.5 nm/10 nm) and the Fe_3O_4 layer (4.5 nm/10 nm) were systematically varied.
- Model dimensions in the X and Z directions were set to >5 nm to eliminate lateral size effects, with the number of atoms ranging from 1.0×10^5 to 1.5×10^5 to ensure statistical validity.
- A five-layer structure (Figure 8) consisting of "fixed layer–cooling layer–phonon collection layer–heating layer–fixed layer" was introduced: the cooling layer (T_{cold} = 710 K) and heating layer (T_{hot} = 730 K) establish a temperature difference

ΔT = 20 K; the phonon collection layer (comprising the three core materials) is used for temperature gradient and heat flux calculations; and the fixed layer prevents rigid body displacement.

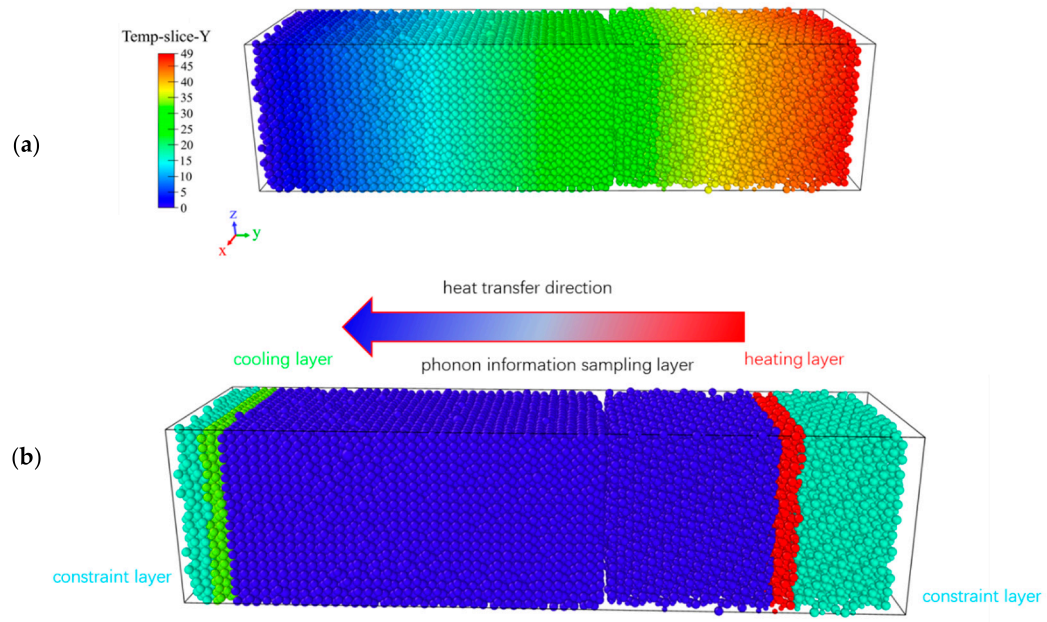

Figure 8. Schematic illustration of thermal conductivity calculations using the NEMD method: (**a**) Temperature statistical binning; (**b**) "Sandwich" structure with different temperature control layers.

Table 2. Design parameters for the T91/Fe-Cr spinel/Fe_3O_4 ternary heterojunction gradient layer thickness model.

Model Number	T91 Layer Thickness/nm	Fe-Cr Spinel Layer Thickness/nm	Fe_3O_4 Layer Thickness/nm	Total Oxide Layer Thickness/nm
M1	10	4.5	3.5	8
M2	10	10	4	14

By applying a temperature difference ($\Delta T = T_{hot} - ot_{cold}$) across the model ends in this manner, a stable, steady-state heat flux is established within the system, flowing from the high-temperature region to the low-temperature region. This symmetrical "heating–cooling" layout ensures uniform heat flux in the central measurement region and prevents boundary effects from penetrating into the interior.

To accurately obtain the temperature distribution along the y-direction and the temperature jump at the interface ($\Delta T_{interface}$), the "phonon collection layer" (i.e., the three-layer material body) is processed using a block-by-block statistical method after the heat flux reaches a steady state. The phonon collection layer is divided into 50 equal slices along the *Y*-axis. Local temperatures are calculated based on atomic velocities, and a linear fit is performed on the temperature points in the bulk region. This fit is then extrapolated to the interface to obtain the temperature jump ΔT_i, thereby eliminating interference from bulk phonon scattering.

In this study, NEMD simulations were conducted at approximately 450 °C (710–730 K), which was selected as the representative temperature. On the one hand, 450 °C is a typical service temperature for T91 steel in lead-cooled fast reactors (LFRs) and represents the midpoint of the experimental temperature range (400–600 °C). Extensive and reliable experimental data on oxide-layer morphology and thermal conductivity were obtained at this temperature, providing a suitable basis for coupling with the simulated

interfacial thermal resistance. On the other hand, the dual-layer oxide structure formed at 450 °C is relatively complete and free from extreme defects, enabling it to accurately reflect the intrinsic interfacial thermal characteristics of the system.

It should be noted that interfacial thermal resistance (ITR) varies with temperature within the range of 400–600 °C. Between 400 °C and 500 °C, increasing porosity and the formation of microcracks within the Fe_3O_4 layer enhance phonon scattering, resulting in a gradual increase in ITR. When the temperature exceeds 550 °C, the densified Fe-Cr spinel layer improves interfacial bonding and consequently reduces ITR. Considering the substantial computational cost associated with MD simulations across the entire temperature range, the ITR value at 450 °C was adopted as a representative parameter for the subsequent multiscale calculations.

3.2. Simulation Results

To ensure statistically reliable interfacial thermal resistance (ITR) values, a rigorous set of numerical procedures was implemented throughout all simulation runs, as detailed below:

1. Prior to the non-equilibrium molecular dynamics (NEMD) heat-transfer calculations, the three-layer interfacial model underwent comprehensive structural and thermal relaxation. Thermal property calculations were initiated only after the entire system had reached a stable equilibrium state, thereby eliminating artifacts arising from structural fluctuations in the calculated thermophysical properties.
2. A dual hot-slab/cold-slab temperature-control scheme was maintained throughout the NEMD simulation process. The heat absorption and heat release rates in the hot and cold regions were continuously monitored on the nanosecond timescale. Steady-state heat flux densities were extracted for subsequent analysis only after a dynamic balance between heat input and heat output had been established, thereby minimizing systematic errors associated with transient heat-flux fluctuations.
3. The simulation domain was divided into uniformly spaced bins along the principal heat-transfer direction to resolve the spatial temperature distribution. A fundamental timestep of 0.5 fs was employed, and data sampling was performed every 100 timesteps, corresponding to a sampling interval of 50 fs. Temperature profiles were generated by averaging data collected over 100 consecutive sampling cycles. Interfacial thermal resistance was calculated only from fully converged temperature fields exhibiting negligible fluctuations at the end of each simulation trajectory, thereby ensuring the statistical reliability and validity of the final ITR results.

3.2.1. Steady-State Heat Flux and Temperature Distribution Evolution

In NEMD simulations, the convergence of steady-state heat flux and temperature distribution is the primary criterion for linear heat transport; both factors jointly ensure the reliability of thermal resistance calculations:

- Steady-state heat flux: After 200 ps, the heat absorption rate of the high-temperature heat source and the heat release rate of the low-temperature heat sink in the M1 and M2 models tend toward equilibrium, resulting in a constant net energy transport flux (Table 3); after 1 ns, the heat flux density reaches a stable plateau, with fluctuations < 2% of the average value, thereby satisfying the "constant heat flux density" assumption of Fourier's law.
- Temperature distribution convergence: As shown in Figure 9, during the initial simulation stage (10 ps), the system exhibits local temperature peaks (energy accumulation). As time progresses (200 ps → 500 ps), these peaks decrease and the spacing between the curves narrows; after 500 ps, the temperature distribution curves of M1 and M2

completely overlap (fluctuation < 10 K). The temperatures in the T91, Fe-Cr spinel, and Fe_3O_4 bulk regions exhibit a strong linear relationship, and the temperature jump ΔT_i at the interface remains stable, indicating that the system has reached thermal equilibrium.

Table 3. Slope of heat flux curves after reaching equilibrium and stabilization.

Indicator/Sample ID	M1	M2
Heat absorption rate (eV/ps)	0.54019	0.45995
Heat release rate (eV/ps)	−0.52785	−0.43205

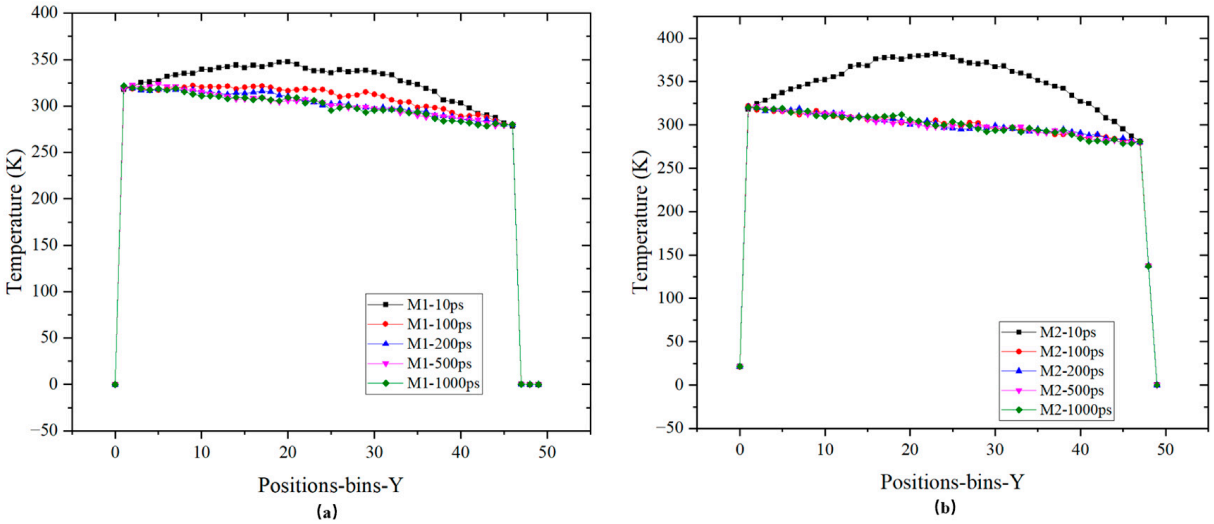

Figure 9. Temperature distribution of the system in the NEMD model at different time steps: (**a**) M1; (**b**) M2.

3.2.2. Calculation and Analysis of Interfacial Thermal Resistance

Based on the steady-state heat flux density (q) and the interfacial temperature jump (ΔT_i), the interfacial thermal resistance was calculated using the formula $R_i = \frac{\Delta T_i \cdot S}{q}$, where S is the cross-sectional area of the model. The key conclusions are as follows (Table 4):

1. Effect of layer thickness on interfacial thermal resistance: The calculated thermal resistance values at the oxide layer interfaces for the two thicknesses are presented in Table 4. For M2 (spinel/Fe_3O_4 layer thickness of 10 nm), the thermal resistance at the T91/spinel interface (R_1) and the spinel/Fe_3O_4 interface (R_2) increased by 13.0% and 5.7%, respectively, compared to M1 (4.5 nm). This increase can be attributed to more pronounced phonon mismatch and significant stress accumulation at the interface within the thicker oxide layer, as well as insufficient relaxation of atomic-scale roughness in the thicker layer.
2. Differences in interface thermal resistance contributions: In both model sets, R_1 is greater than R_2 (M1: $R_1 = 2.3 \times 10^{-8}$ m$^2 \cdot$ K/W, $R_2 = 1.8 \times 10^{-8}$ m$^2 \cdot$ K/W). This is because the difference in phonon spectra between the metal (T91) and the oxide (spinel) is greater than that between the two oxides, resulting in lower phonon transmission efficiency.

Table 4. Calculated results for the interfacial thermal resistance of models with different layer thicknesses.

Model Number	R_1 (T91/Fe-Cr Spinel)/10^{-9} $m^2 \cdot K/W$	R_2 (Fe-Cr Spinel/Fe_3O_4)/10^{-9} $m^2 \cdot K/W$
M1	3.15	2.96
M2	3.56	3.13

4. Calculation of Thermal Conductivity for Fe_3O_4 and Fe-Cr Spinel

MD simulations can accurately describe heat transport processes at solid–solid interfaces at the atomic scale. By constructing atomically flat ideal interface models and using the NEMD method, the intrinsic interfacial thermal resistance between materials can be calculated. This method has been widely applied to systems, such as metal/oxide and two-dimensional materials/substrate interfaces, and it provides reliable input parameters for macroscopic thermal resistance models.

Zhang et al. [18] established a multiscale thermal simulation framework spanning from the atomic to the device scale. They used NEMD simulations to calculate the interfacial thermal resistance R between two-dimensional materials, such as phosphorene and silicene, and dielectric substrates, such as SiO_2 and TiO_2. The results were found to be close to the thermal resistance at the graphene/SiO_2 interface and insensitive to temperature. Subsequently, these MD results were used as input parameters for device-scale finite element simulations to analyze the temperature distribution and thermal dissipation performance of transistors.

Zhang et al. [19] combined MD-calculated interfacial thermal resistance with a macroscopic porous medium model, thereby verifying the applicability of MD results in macroscopic thermal calculations. This study focused on a PVDF/SiO_2 bilayer composite film, using MD simulations to obtain the thermal conductivity of the solid matrix and the interfacial thermal resistance between layers. By integrating these results with a macroscopic porous medium resistance model, the effective thermal conductivity of the composite film was calculated.

Steady-state heat conduction in multilayer materials along the thickness direction can be described using a series thermal resistance model. For a multilayer structure composed of a T91 matrix, an Fe-Cr spinel layer, and an Fe_3O_4 layer, the total thermal resistance can be expressed as the sum of the thermal resistances of each component and the interfacial thermal resistance:

$$R_{\text{total}} = \frac{L_{\text{T91}}}{\kappa_{\text{T91}}} + \frac{L_s}{\kappa_s} + \frac{L_m}{\kappa_m} + R_{\text{int}} \quad (1)$$

where L represents the thickness of each layer (unit: μm), κ represents the thermal conductivity (unit: W/(m·K)), and the subscripts T91, s, m denote the T91 matrix, the Fe-Cr spinel layer, and the Fe_3O_4 layer, respectively; R_{int} is the sum of the thermal resistances at the T91/spinel and spinel/Fe_3O_4 interfaces.

This study uses experimental data from two sets with different oxide layer thicknesses for simultaneous solution (corrosion for 1000 h at 450 °C and 400 °C in an LBE alloy with an oxygen concentration of 1×10^{-6} wt.%) to determine the macroscopic effective thermal conductivities of the Fe-Cr spinel layer and the Fe_3O_4 layer. The total thermal conductivity of the T91 matrix and the samples was obtained from actual measurements: $\kappa_{\text{T91}} = 26.623\ \text{W}/(\text{m}\cdot\text{K})$. The geometric parameters and interfacial thermal resistance data for the two sets of conditions are listed in Table 5. The thickness ratio of the Fe-Cr spinel layer to the Fe_3O_4 layer obtained from the MD simulation is consistent with that obtained from the actual corrosion experiments.

Table 5. Experimental parameters and calculation results.

Operating Condition	L_s (μm)	L_m (μm)	κ_{total} (W/(m·K))	R_{int} ($\times 10^{-9}$ m^2·K/W)	R_{ox} ($\times 10^{-6}$ m^2·K/W)
1	10.0	4.0	24.29317	6.69	7.78
2	4.5	3.5	25.2897	6.11	4.28

The total thermal resistance is calculated based on the bulk thermal conductivity and total thickness:

$$R_{\text{total}} = \frac{L_{\text{T91}} + L_s + L_m}{\kappa_{\text{total}}} \tag{2}$$

The volumetric thermal resistance of the T91 matrix is:

$$R_{\text{T91}} = \frac{L_{\text{T91}}}{\kappa_{\text{T91}}} = 7.5123 \times 10^{-5}\ \text{m}^2\text{K/W} \tag{3}$$

The sum of the bulk thermal resistances of the oxide layers (spinel + Fe_3O_4) is obtained by subtracting the bulk thermal resistance of T91 and the interfacial thermal resistance from the total thermal resistance:

$$R_{\text{ox}} = R_{\text{total}} - R_{\text{T91}} - R_{\text{int}} \tag{4}$$

The calculation results are listed in the last column of Table 5. Let $x = 1/\kappa_s$ and $y = 1/\kappa_m$. Based on the two operating conditions, a system of equations for the thermal conductivities of the spinel layer and the Fe_3O_4 layer can be established, yielding $x \approx 0.5954$ and $y \approx 0.4565$. From this, the following results are obtained:

$$\kappa_s = 1/x \approx 1.68\ \text{W/(m·K)}, \kappa_m = 1/y \approx 2.19\ \text{W/(m·K)} \tag{5}$$

The results are lower than those reported by Beygelzimer and Beygelzimer [20], Li et al. [21], Slack [22], and Liu et al. [23]. This discrepancy arises primarily because the thermal conductivities cited in the literature correspond to pure-phase materials. In actual corrosion processes, the Fe-Cr spinel layer and Fe_3O_4 layer typically develop defects, such as porosity, which leads to a reduction in thermal conductivity.

5. Mechanism of Corrosion Environment Influence on the Thermal Conductivity of Structural Materials

5.1. Thermal Conductivity of T91 Before Corrosion

Before preparing the corrosion specimens, five T91 specimens were taken from different locations within the same batch of steel. Their thermal conductivities were measured at 350 °C, 400 °C, 450 °C, and 500 °C. The pre-corrosion thermal conductivities of T91 are presented in Table 6. The thermal conductivity of T91 decreases from 27.092 W/(m·K) (350 °C) to 25.101 W/(m·K) (500 °C) over the temperature range of 350 °C to 500 °C.

Table 6. Thermal conductivity of T91 before corrosion.

Temperature (°C)	Thermal Conductivity (W/(m·K))
350	27.092
400	27.062
450	26.623
500	25.101

To ensure the reliability and reproducibility of the test data, three measurement locations were selected on each specimen, and each location was tested three times. The

arithmetic mean of the three measurements was used as the thermal conductivity value for the corresponding specimen. As reported in the literature [24], the laser flash method provides high precision and reliability over a wide temperature range and under various experimental conditions. Based on validation using reference materials, its repeatability and reproducibility are approximately ±1%, while its accuracy ranges from 3% to 5%. In addition, the instrument software automatically reports the statistical precision (repeatability) and the combined measurement uncertainty for each test. Statistical analysis of the present experimental data indicated a maximum uncertainty of 0.4% and a maximum standard deviation of 4.8%.

5.2. Effect of Corrosion Temperature on Thermal Conductivity

For each specimen group, the oxide-layer thickness was measured at three randomly selected independent locations on cross-sectional SEM micrographs. The arithmetic mean of the three sets of thickness measurements was used as the representative oxide-layer thickness for the corresponding specimen. All raw thickness measurements were consistently rounded to one decimal place.

After 1000 h of corrosion at different temperatures (400 °C, 450 °C, 500 °C, and 550 °C) and an oxygen concentration of 1×10^{-6} wt.% in an LBE alloy (55.5% Bi), the characteristics of the T91 oxide layer and its thermal conductivity are presented in Table 7. After corrosion, T91 forms a continuous oxide layer, the thickness of which gradually increases. The thermal conductivity exhibits a non-monotonic trend of "initial decrease followed by an increase" with increasing corrosion temperature. It decreases continuously between 400 °C and 500 °C, and although the oxide layer continues to thicken at 550 °C, the thermal conductivity exhibits a slight recovery.

Table 7. Thermal conductivity of T91 at different corrosion temperatures.

Corrosion Temperature (°C)	Number of Oxidation Layers	Oxidation Layer Thickness (μm)	Oxidation Layer Condition	Thermal Conductivity (W/(m·K))
400	2	4.5	Continuous, with an outer Fe_3O_4 layer 2.5 μm thick and an inner Fe-Cr spinel layer 2 μm thick	26.115
450	2	8	Continuous, outer Fe_3O_4 layer 4.5 μm, inner Fe-Cr spinel layer 3.5 μm, with a small amount of PbBi entering the oxide layer	25.290
500	2	14	Continuous, with an outer Fe_3O_4 layer 10 μm thick (porous, with slight delamination) and an inner Fe-Cr spinel layer 4 μm thick	24.293
550	2	18	Continuous, dense; outer Fe_3O_4 layer thickness: 3 μm; inner Fe-Cr spinel layer thickness: 15 μm	24.380

Using 450 °C as the uniform reference measurement temperature, as shown in Figure 10, after 1000 h of corrosion in an LBE alloy with an oxygen concentration of 1×10^{-6} wt.% and a Bi mass fraction of 55.5%, a continuous double-layer oxide structure consisting of an outer Fe_3O_4 layer and an inner Fe-Cr spinel layer formed on the T91 surface, with no obvious discontinuities or local defects. The total thickness of the oxide layer increased continuously from 4.5 μm to 18 μm as the corrosion temperature (400–550 °C) increased, and the thermal conductivity exhibited a trend of initial decrease followed by an increase as the structure evolved.

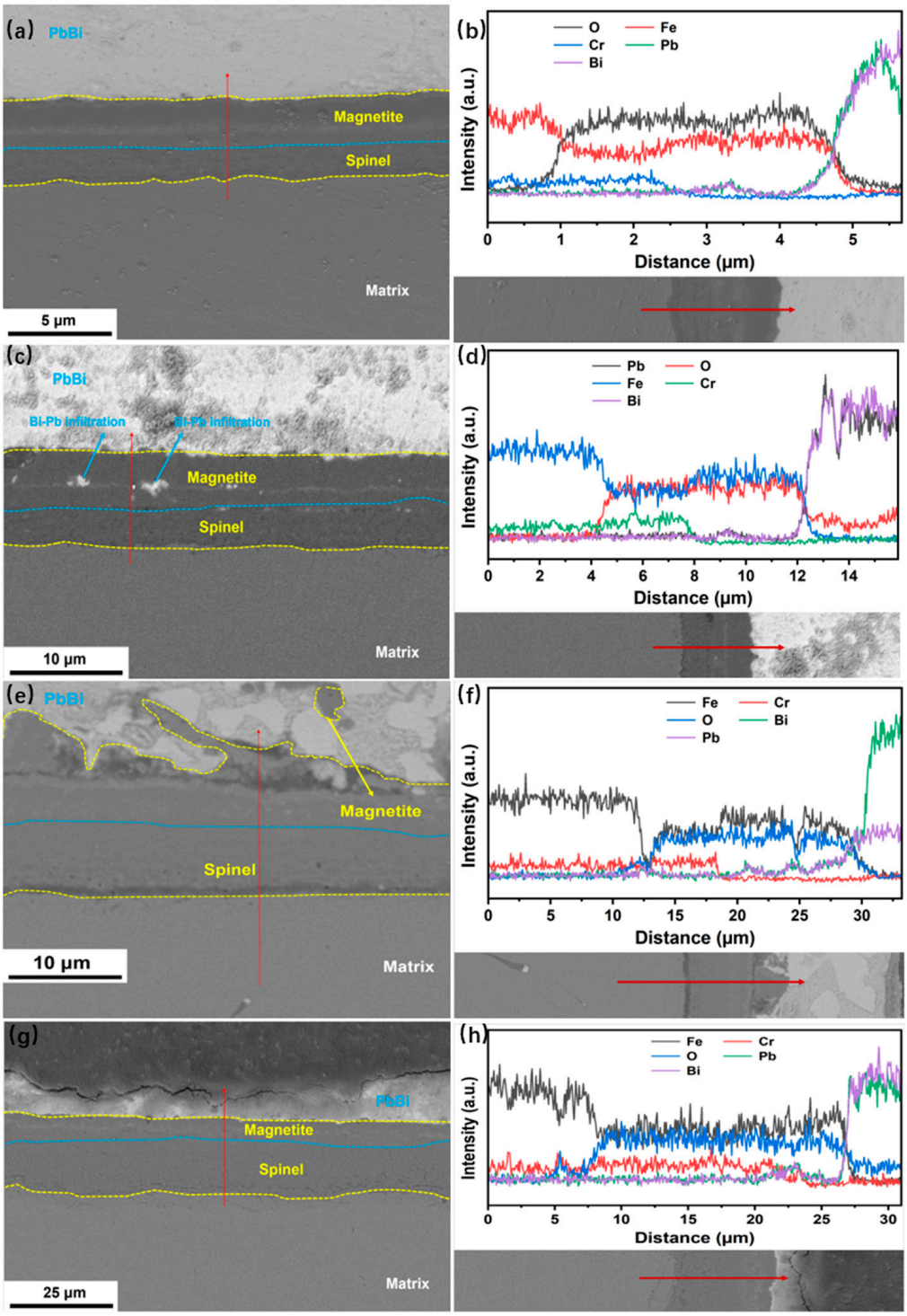

Figure 10. SEM cross-sectional morphology and EDS line scan spectra of T91 after 1000 h of corrosion in a 1×10^{-6} wt.% oxygen concentration and a lead–bismuth alloy (55.5% Bi): (**a**,**b**) 400 °C; (**c**,**d**) 450 °C; (**e**,**f**) 500 °C; (**g**,**h**) 550 °C.

At 400 °C, the oxide layer exhibited a continuous, dense, two-layer structure consisting of an outer Fe_3O_4 layer (2.5 μm) and an inner Fe-Cr spinel layer (2 μm), with a thermal conductivity of 26.115 W/(m·K), representing a 2% decrease compared to the uncorroded state. At 450 °C, the thickness of the oxide layer increased to 8.5 μm (Fe_3O_4 4.5 μm, spinel 4 μm), with a small amount of PbBi diffusing inward to form localized microdefects; the thermal conductivity decreased to 25.290 W/(m·K), corresponding to a reduction of 5%. At 500 °C, the total thickness of the oxide layer reached 14 μm, with the outer Fe_3O_4 layer

increasing to 10 μm (71.4% of the total). It became loose and porous, exhibiting localized delamination, while the inner spinel layer remained at 4 μm. The increased proportion of low-thermal-conductivity Fe_3O_4, the introduction of pores (the loose structure of the outer Fe_3O_4 layer and its tendency to detach from the substrate can be clearly observed in Figure 10e), and the superposition of interfacial thermal resistance enhanced phonon scattering, resulting in a thermal conductivity of 24.293 W/(m·K), a decrease of 8.8%.

At 550 °C, the structure of the oxide layer was significantly optimized: the inner spinel layer increased to 15 μm (accounting for 83.3%), with improved density and reduced porosity; the outer Fe_3O_4 layer was reduced to 3 μm, exhibiting improved uniformity without delamination and with strong interfacial bonding. The higher-thermal-conductivity spinel became the dominant phase, reducing phonon scattering and lowering interfacial thermal resistance, thereby offsetting the increase in thermal resistance due to thickness. The thermal conductivity recovered to 24.380 W/(m·K), with the decrease narrowing to 8.4%, representing an increase of 0.087 W/(m·K) compared to 500 °C.

The EDS area scan results in Figure 11 show that at 500 °C, there is strong enrichment of Fe and O in the outer layer, while the Cr signal is weak, corresponding to a porous Fe_3O_4 layer. In the inner layer, Cr, Fe, and O are co-enriched to form a spinel phase, with a small amount of PbBi diffusing into the pores of the outer layer. The porous structure and microcracks in the oxide layer act as thermal barriers that hinder heat transfer. Figure 12 shows that at 550 °C, Cr is continuously and uniformly enriched in the inner layer, corresponding to a dense spinel phase; Fe and O in the outer layer are concentrated only within an extremely thin region, and PbBi penetration is significantly suppressed. The gradual transition of elements at the interface confirms the mechanism of oxide layer structural optimization and the recovery of thermal conductivity.

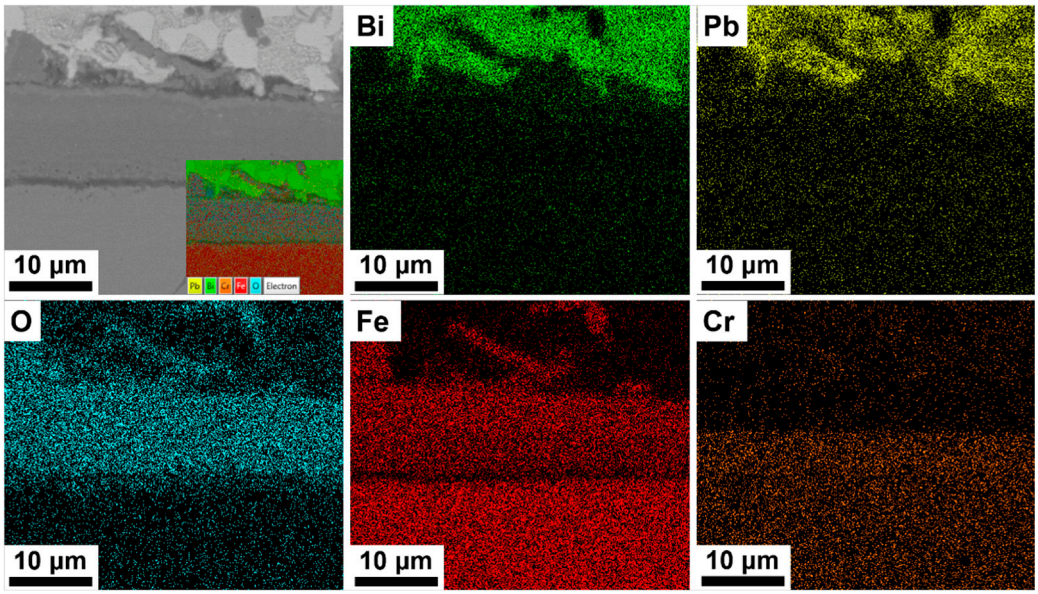

Figure 11. EDS surface scan of T91 after 1000 h of corrosion at 500 °C, 1 × 10^{-6} wt.% oxygen concentration, in a lead–bismuth alloy (55.5% Bi).

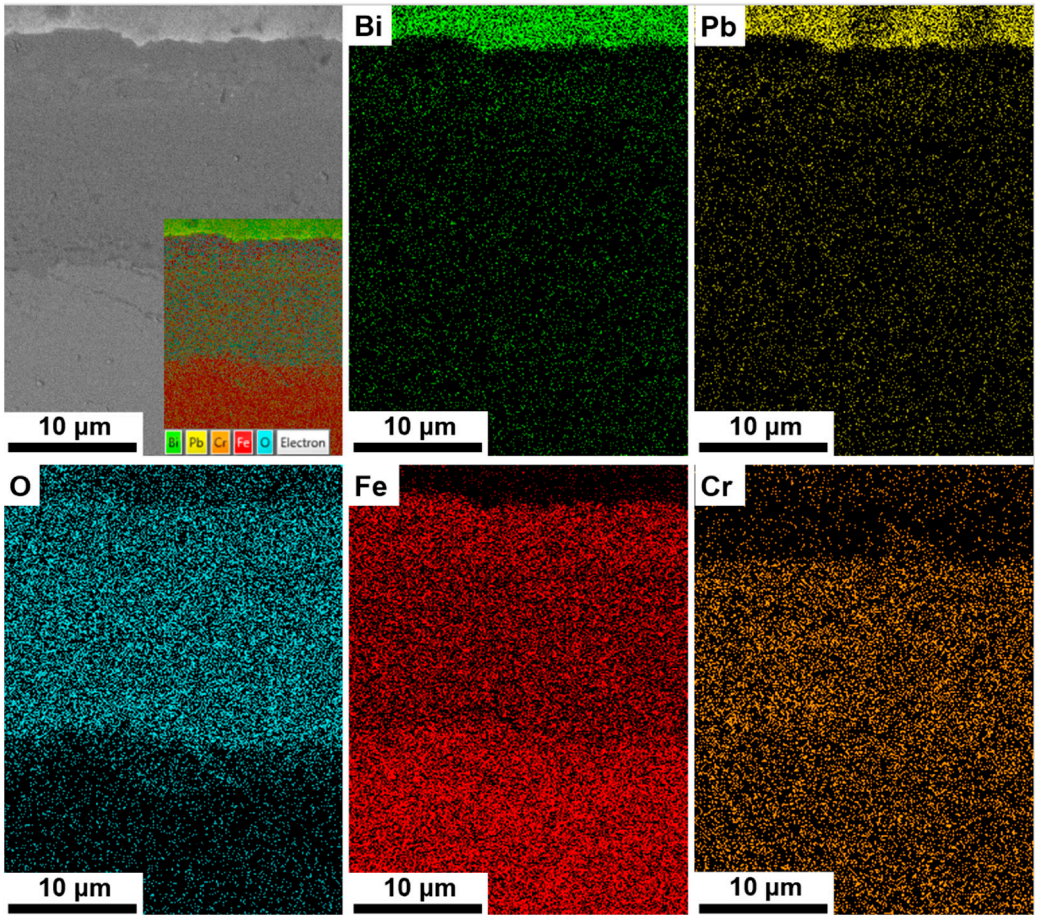

Figure 12. EDS surface scan of T91 after 1000 h of corrosion at 550 °C, 1 × 10^{-6} wt.% oxygen concentration, in a lead–bismuth alloy (55.5% Bi).

It is necessary to clarify that the intrinsic thermal conductivity of Fe-Cr spinel (1.68 W/(m·K)) is lower than that of Fe_3O_4 (2.19 W/(m·K)). The recovery of thermal conductivity at 550 °C cannot be simply attributed to the change in phase proportion. At 500 °C, the Fe_3O_4 layer accounts for 71.4% of the total oxide thickness. The loose structure, abundant micropores and local delamination inside this layer generate high interfacial thermal resistance and seriously impede heat transfer. At 550 °C, the proportion of Fe-Cr spinel increases to 83.3%. The spinel layer formed at this temperature is dense with reduced porosity and no delamination, and the interfacial bonding between layers is well optimized. According to the series thermal resistance model used in this study, the total thermal resistance of the multilayer oxide structure includes both bulk thermal resistance and interfacial thermal resistance. The significant reduction in micro-defects and interfacial thermal resistance plays a leading role in improving heat transfer performance. This positive effect exceeds the adverse impact caused by the relatively low intrinsic thermal conductivity of Fe-Cr spinel, which explains the recovery of the overall thermal conductivity of T91 steel at 550 °C.

5.3. Effect of Corrosion Time on Thermal Conductivity

Table 8 presents the characteristics of the oxide layer and the thermal conductivity of T91 after 1000 h, 2500 h, 4000 h, 5000 h, and 9000 h of corrosion in an LBE alloy (Bi content 55.5%) at 450 °C and an oxygen concentration of 1 × 10^{-6} wt.%.

Table 8. Thermal conductivity of T91 after different corrosion durations.

Corrosion Time (h)	Number of Oxide Layers	Oxide Layer Thickness (μm)	Oxide Layer Condition	Thermal Conductivity (W/(m·K))
1000	2	8	Continuous, with an outer Fe_3O_4 layer 4.5 μm thick and an inner Fe-Cr spinel layer 3.5 μm thick	25.290
2500	2	10	Continuous, with an outer Fe_3O_4 layer 4.5 μm thick and an inner Fe-Cr spinel layer 5.5 μm thick; the inner layer exhibits a layered structure	23.078
4000	2	16	Continuous, with delamination between the oxide layer and the substrate; the outer Fe_3O_4 layer is more porous than the inner layer, with a thickness of 6 μm, and the inner Fe-Cr spinel layer has a thickness of 10 μm	22.072
5000	2	18.8	Continuous; the outer Fe_3O_4 layer is 10 μm thick, and the inner Fe-Cr spinel layer is 8.8 μm thick	22.813
9000	2	8.7	Continuous, with an outer Fe_3O_4 layer 1.7 μm thick and an inner Fe-Cr spinel layer 7 μm thick	25.072

T91 exhibits a nonlinear evolution in thermal conductivity, characterized by a "continuous decline—drop to a minimum—significant rebound—tendency toward recovery" (25.289 W/(m·K) → 23.078 W/(m·K) → 22.072 W/(m·K) → 22.813 W/(m·K) → 25.072 W/(m·K)). This evolution is primarily driven by dynamic changes in the thermal resistance of the oxide layer, the evolution of thermal resistance at the substrate–oxide interface, variations in the structural integrity and phase distribution of the oxide layer, and the degradation of heat transport caused by LBE medium penetration.

After 1000 h of corrosion, a continuous double-layer oxide layer formed on the T91 surface (total thickness 8 μm), with an outer layer of Fe_3O_4 (4.5 μm) and an inner layer of dense Fe-Cr spinel (3.5 μm). The substrate and oxide layer were tightly bonded, and only a small amount of LBE penetrated into the outer Fe_3O_4 layer (Figure 13a,b). At this stage, the thermal resistance of the oxide layer is the primary factor contributing to the deterioration of thermal conductivity; however, due to its relatively small total thickness, the thermal conductivity remains at a relatively high level, decreasing by 5.01% compared to the pre-corrosion state.

After 2500 h of corrosion (Figure 13c,d), the total thickness of the oxide layer increased to 10 μm, and the inner Fe-Cr spinel layer thickened to 5.5 μm, developing a layered structure that increased the number of thermal scattering interfaces within the spinel layer. The increased thickness of the oxide layer caused the total thermal resistance to rise, and the thermal conductivity decreased to 23.078 W/(m·K).

At 4000 h, the thermal conductivity reached its lowest value for the entire cycle (22.0723 W/(m·K)), primarily due to the coupled effects of oxide layer structural degradation and a sharp increase in interfacial thermal resistance. At this stage, the total thickness of the oxide layer reached 16 μm, and in some regions, the oxide layer and substrate exhibited significant separation, forming micron-scale gaps and resulting in an order-of-magnitude increase in thermal resistance at the substrate–oxide interface. The interfacial gaps, internal micropores, and microcracks formed during long-term corrosion serve as major structural

defects, leading to a sharp drop in thermal conductivity. Combined with the EDS line scan results (Figure 13e,f), the increased oxide layer thickness and the separation between the substrate and oxide layer jointly caused the total thermal resistance to reach its peak, while the thermal conductivity dropped to its minimum value.

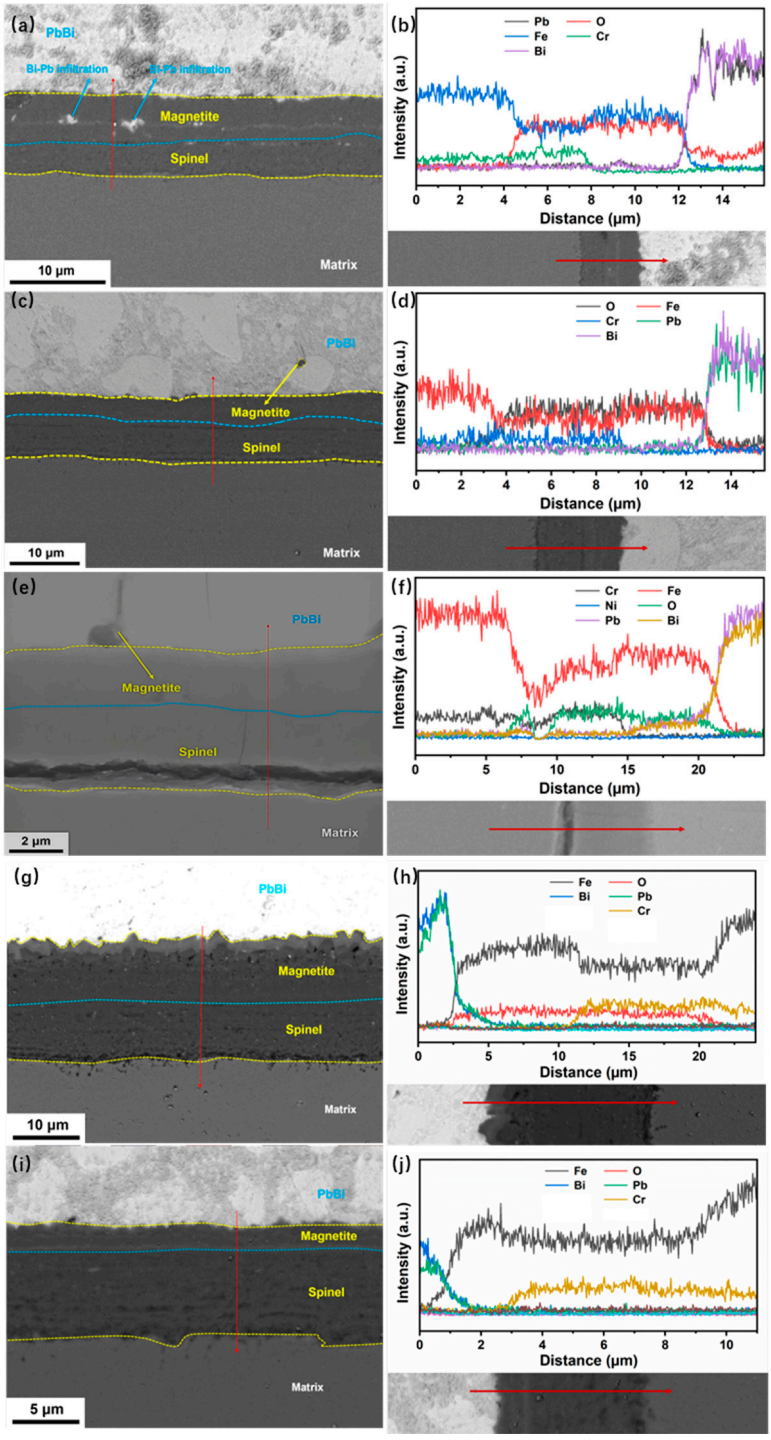

Figure 13. SEM cross-sectional morphologies and EDS line scan spectra of T91 after corrosion at 450 °C in 1×10^{-6} wt.% oxygen concentration and a lead–bismuth alloy (55.5% Bi): (**a**,**b**) 1000 h-Note that the image for the control group is identical to that in Figure 10c,d, presented here to facilitate direct comparison across different experimental conditions; (**c**,**d**) 2500 h (**e**,**f**) 4000 h; (**g**,**h**) 5000 h; (**i**,**j**) 9000 h.

At 5000 h, the thermal conductivity recovered to 22.813 W/(m·K). Although the total thickness of the oxide layer further increased to 18.8 μm, the structural integrity of the oxide layer—specifically, the absence of gaps—became the key factor driving this recovery in thermal conductivity. At this stage, the oxide layer consisted of a continuous three-layer structure with no gaps between the substrate and the oxide layer, resulting in a significant reduction in interfacial thermal resistance. EDS line scans (Figure 13g,h) show that the outer layer is enriched in Fe, O, Pb, and Bi, consisting of $PbFe_4O_7$ and elemental Bi, with a thermal conductivity slightly higher than that of the oxide layer. The dense Fe-Cr spinel layer in the middle serves as the primary resistance layer for heat transport; its structural integrity partially offsets the negative impact of increased oxide layer thickness, resulting in a lower total thermal resistance compared to that at 4000 h and a slight recovery in thermal conductivity.

At 9000 h, the thermal conductivity further recovered to 25.072 W/(m·K), approaching the level at the onset of corrosion. The primary reason is a significant reduction in total thermal resistance due to the peeling of the oxide layer. At this stage, the oxide layer underwent pronounced selective peeling. EDS line scans (Figure 13i,j) show that the total thickness decreased to 8.7 μm (equivalent to that at 1000 h), with the outer Fe_3O_4 layer measuring only 1.7 μm and the inner Fe-Cr spinel layer 7 μm. The substantial reduction in oxide layer thickness directly lowered the intrinsic thermal resistance of the oxide, while the dense spinel layer remained tightly bonded to the substrate, maintaining a low interfacial thermal resistance. Although the thickness of the inner spinel layer was slightly lower than that at 5000 h, the total thermal resistance of the oxide layer decreased to a level close than that at the initial stage, ultimately restoring the thermal conductivity to 25.072 W/(m·K).

5.4. Effect of Bi Content on Thermal Conductivity

After 1000 h of corrosion at 600 °C, under saturated oxygen concentration and varying Bi contents (50 wt.%, 55.5 wt.%, 57 wt.%) in the environment, the characteristics of the T91 oxide layer and its thermal conductivity are presented in Table 9. The relationship between temperature and thermal conductivity is illustrated in Figure 13.

Table 9. Thermal conductivity of T91 after corrosion at different bismuth contents.

Bi Content (wt.%)	Number of Oxide Layers	Oxide Layer Thickness (μm)	Oxidation Layer Condition	Thermal Conductivity (W/(m·K))
50	3	30	The outer Fe_3O_4 layer is 17 μm thick, the spinel layer is 8 μm thick, and the IOZ layer is 5 μm thick.	24.266
55.5	3	47	The outer $PbFe_4O_7$+ Bi layer is 8 μm thick, the Fe_3O_4 layer is 17 μm thick, the spinel layer is 15 μm thick, and the IOZ layer is 7 μm thick.	23.710
57	3	48	The outer $PbFe_4O_7$+ Bi layer is 6 μm thick, the Fe_3O_4 layer is 19 μm thick, the spinel layer is 16 μm thick, and the IOZ layer is 7 μm thick.	23.141

The thermal conductivity of T91 exhibits a continuous decrease with increasing Bi content, with a diminishing rate of decline, decreasing from 24.266 W/(m·K) at 50 wt.% to 23.710 W/(m·K) at 55.5 wt.%, and further to 23.141 W/(m·K) at 57 wt.%. This behavior arises from the combined effects of structural transformation and thickness evolution of the oxide layer, with the dominant factors varying significantly at different stages.

Figure 14 shows the cross-sectional morphology of the oxide layer on T91 after 1000 h of corrosion in LBE alloys with different Bi contents. It can be observed that a continuous layered oxide structure formed on the surface of all three of the samples, and the thickness of the oxide layer increased with increasing Bi content.

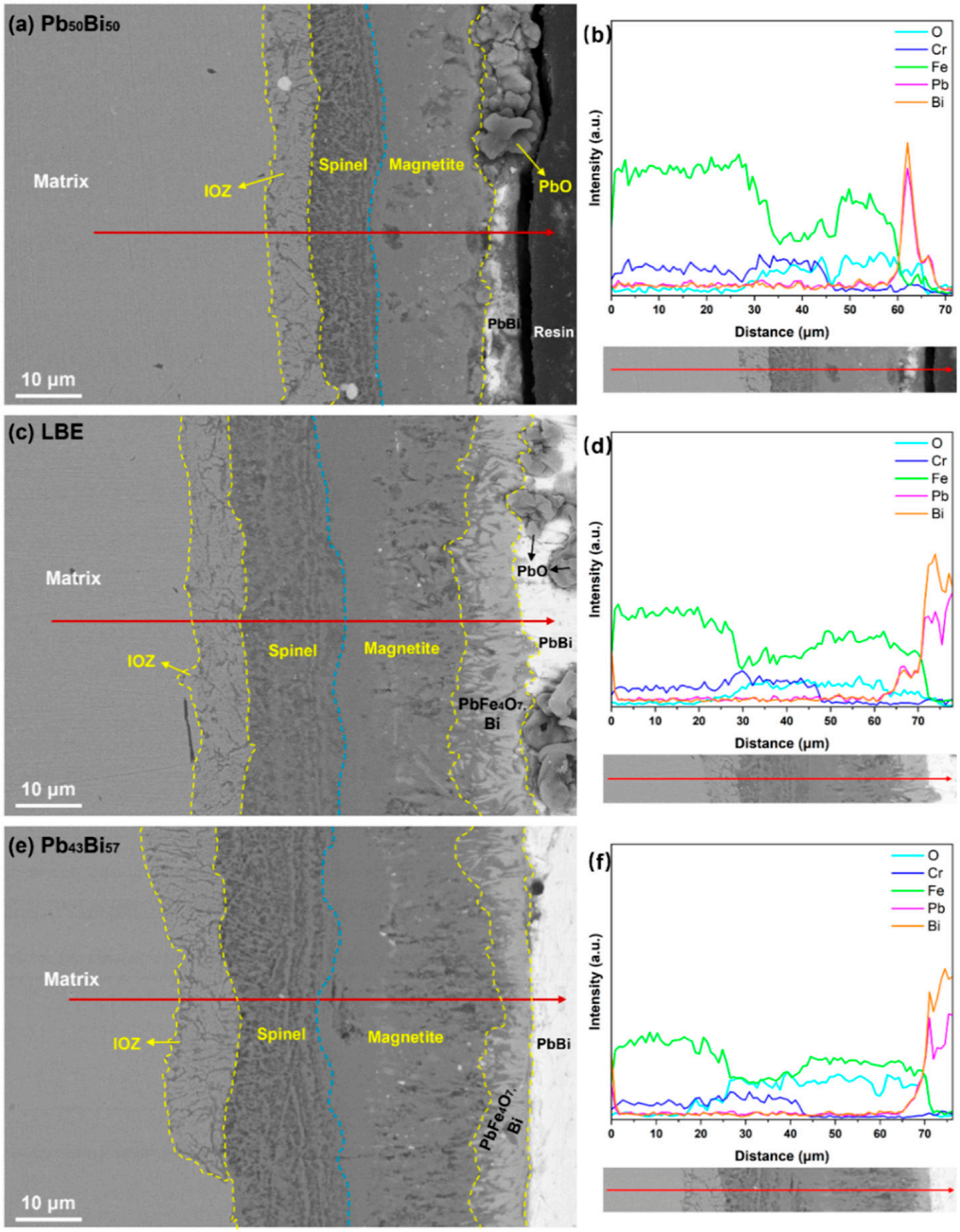

Figure 14. SEM cross-sectional morphology and elemental analysis of T91 after 1000 h of corrosion in 600 °C saturated oxygen: Pb50Bi50 (**a**,**b**), LBE (**c**,**d**), and Pb43Bi57 (**e**,**f**) alloys.

As shown in Figure 14a, after corrosion in the Pb50Bi50 alloy, a three-layer oxide structure formed on the T91 surface from the inside outward. A non-uniform oxide layer with a thickness of approximately 5 μm was observed in the region immediately adjacent to the T91 matrix. EDS line scan results show that the Fe content in this layer decreases from the inside outward, while the Cr and O contents increase (Figure 14b), indicating that this is the IOZ layer. A dark gray oxide layer with a thickness of approximately 8 μm was observed in the intermediate region adjacent to the IOZ layer. EDS line scan results

indicate that this dark gray oxide layer is enriched in Fe, Cr, and O elements, suggesting that it corresponds to the Fe-Cr spinel. Both the IOZ and Fe-Cr spinel layers are oxide layers formed in situ by the diffusion of oxygen into the steel matrix. In addition, a gray oxide layer with a thickness of approximately 17 μm is present in the outermost region adjacent to PbBi. EDS line scan results confirm that this gray oxide layer is enriched in Fe and O, indicating that it corresponds to Fe_3O_4.

As shown in Figure 14c, when the Bi content increases from 50 wt.% to 55.5 wt.%, the cross-sectional morphology of the oxide layer undergoes a significant transformation. On the steel surface, from the inside outward, in addition to the IOZ, Fe-Cr spinel, and Fe_3O_4 layers, a light gray oxide layer with a thickness of approximately 8 μm is observed in the outermost region adjacent to PbBi. EDS results confirm that this layer is enriched in Fe, O, Pb, and Bi (Figure 14d), consisting of $PbFe_4O_7$ and elemental Bi. At this stage, the thermal conductivity decreased by 0.556 W/(m·K) compared to the 50 wt.% case. The primary reasons for this decrease include the formation of a four-layer structure and the increase in oxide layer thickness; the newly formed low-thermal-conductivity phase, the $PbFe_4O_7$+ Bi layer, is the dominant contributor to thermal resistance. The thermal conductivity of $PbFe_4O_7$ at 600 °C is only 1.8 W/(m·K) to 2.5 W/(m·K), which is lower than that of Fe_3O_4 and Fe-Cr spinel; even with a layer thickness of only 8 μm, it significantly increases the average thermal resistance of the oxide layer. In addition, the total thickness of the oxide layer increased from 30 μm to 47 μm, representing a 56.7% increase. Since the thermal conductivity of the T91 matrix is much higher than that of the various oxide phases, the increase in thickness directly lengthens the heat conduction path, leading to a nonlinear increase in overall thermal resistance.

When the Bi content increased to 57 wt.%, the structure of the oxide layer became similar to that formed in LBE, also consisting of four layers: the IOZ layer, Fe-Cr spinel, Fe_3O_4 layer, and $PbFe_4O_7$+ Bi layer (Figure 14e,f); however, discontinuities appeared in the IOZ layer. At this stage, the thermal conductivity decreased by 0.569 W/(m·K), with the dominant factors shifting to a slight increase in oxide layer thickness and an increase in interfacial thermal resistance caused by discontinuities in the IOZ layer. The total thickness of the oxide layer increased by only 1 μm, contributing minimally to the increase in thermal resistance. Meanwhile, the thickness of the $PbFe_4O_7$+ Bi layer decreased from 8 μm to 6 μm, partially offsetting the increase in thermal resistance caused by the slight increase in overall thickness. The discontinuities in the IOZ layer also led to the formation of numerous discontinuous interfaces between the IOZ and the substrate, as well as between the IOZ and the Fe-Cr spinel layer. This significantly enhanced phonon scattering at these interfaces during heat conduction, introducing additional interfacial thermal resistance. The combined effect resulted in a slight decrease in thermal conductivity. The newly generated pores and microcracks further aggravate phonon scattering, which is an important cause of the continuous decline of thermal conductivity with an increasing Bi content.

6. Conclusions

1. Patterns of oxide layer evolution: After corrosion of T91 in an LBE environment, a double- or multilayer oxide structure primarily composed of Fe-Cr spinel and Fe_3O_4 forms on the surface. The thickness of the oxide layer generally increases with increasing temperature, time, and Bi content; however, the phase composition, density, and interfacial bonding state are significantly influenced by corrosion conditions. Below 500 °C, growth of the outer Fe_3O_4 layer dominates; at 550 °C, the inner spinel layer becomes the dominant phase and its density increases; and after more than 5000 h of corrosion, structural repair and selective peeling occur in the oxide layer;

increased Bi content induces the formation of the low-thermal-conductivity $PbFe_4O_7$ phase and alters the multilayer structure of the oxide layer.

2. Nonlinear evolution mechanism of thermal conductivity: The overall thermal conductivity of T91 exhibits a non-monotonic variation with corrosion temperature, time, and Bi content. With respect to temperature, thermal conductivity continuously decreases between 400 °C and 500 °C, then rebounds at 550 °C due to the increased proportion of the inner spinel layer and structural densification. With respect to time, thermal conductivity follows a "decrease–minimum–recovery–near recovery" trajectory, with oxide layer exfoliation and retention of the dense spinel layer being the primary factors driving the later recovery of thermal conductivity. Regarding Bi content, thermal conductivity decreases continuously with increasing Bi content, although the rate of decrease gradually diminishes, with the formation of the $PbFe_4O_7$ phase and interfacial discontinuities being the main contributing factors.
3. Interfacial thermal resistance dominates heat transport: NEMD simulation results based on the NEP indicate that the interfacial thermal resistances for the T91/Fe-Cr spinel and Fe-Cr spinel/Fe_3O_4 interfaces are 3.15×10^{-9} and 3.56×10^{-9} $m^2 \cdot K/W$, and 2.96×10^{-9} and 3.13×10^{-9} $m^2 \cdot K/W$, respectively, with the former being significantly higher than the latter due to greater phonon spectrum mismatch between the metal and the oxide.
4. Calculation of effective thermal conductivity of the oxide layer: By combining experimental data from two sets with different oxide layer thicknesses with interfacial thermal resistances obtained from MD simulations, and solving based on a series thermal resistance model, the macroscopic effective thermal conductivities of Fe-Cr spinel and Fe_3O_4 in a corrosive environment were determined to be 1.68 W/(m·K) and 2.19 W/(m·K), respectively. These values are significantly lower than literature values for pure-phase thermal conductivity, reflecting the additional inhibitory effects on heat transport caused by defects, such as pores, microcracks, and elemental gradients in actual oxide layers.
5. Validity of the multiscale approach: The multiscale analytical framework established in this study—comprising corrosion experiments, microscopic characterization, MD-based interfacial thermal resistance calculations, and a macroscopic series thermal resistance model—enables a comprehensive investigation spanning from interfacial heat transport mechanisms at the atomic scale to the evolution of macroscopic thermal conductivity. This provides a generalizable methodological foundation for the accurate prediction of thermal properties of structural materials under complex corrosion environments.

Author Contributions: Conceptualization, X.G., X.Z. and Z.S.; Investigation, X.G. and Z.S.; Formal Analysis, X.G. and Z.S.; Software, X.Z.; Data Curation, X.G.; Visualization, X.G.; Writing—Original Draft Preparation, X.G.; Writing—Review & Editing, X.Z. All authors have read and agreed to the published version of the manuscript.

Funding: This research received no external funding.

Data Availability Statement: The original contributions presented in this study are included in the article. Further inquiries can be directed to the corresponding author.

Acknowledgments: The authors sincerely thank Xian Zeng for valuable guidance on lead–bismuth corrosion characterization and molecular dynamics simulations. The authors also express their gratitude to their colleagues for their generous assistance and continuous support throughout this study.

Conflicts of Interest: The authors declare no conflicts of interest. Author Xian Zeng, Zhaoxuan Sun was employed by China Nuclear Power Technology Research Institute Co., Ltd. The remaining authors declare that the research was conducted in the absence of any commercial or financial relationships that could be construed as a potential conflict of interest.

References

1. Cai, Y.; Zhang, D.; Lin, Y.; Du, P.; Wang, B.; Zhu, L.; Tian, W.; Qiu, S.; Su, G. Thermal-hydraulics analysis of a small lead-cooled fast reactor with reactor vessel cooling system using ACENA. *Ann. Nucl. Energy* **2026**, *227*, 111925. [CrossRef]
2. Li, Q.; Cai, S.; Zhang, S.; Liu, X.; Zhang, N.; Hu, C.; Zeng, X.; Sun, J.; Cai, W. Numerical study on heat transfer enhancement of LBE flow in semicircular-fin fuel bundles. *Prog. Nucl. Energy* **2026**, *194*, 106253. [CrossRef]
3. Zhang, M.; He, G.; Scales, R.; Song, K.; Lapington, M.; Zhou, W.; Ding, Z.; Short, M.P.; Bagot, P.A.; Moody, M.P.; et al. Correlated chromium carbide dissociation and phase transformation in liquid lead-bismuth eutectic corroded T91 steel. *Corros. Sci.* **2025**, *249*, 112851. [CrossRef]
4. Lin, Q.; Zhao, W.; Liu, Z.; Hu, J.; Chen, G.; Feng, S.; Shi, S. High-cycle fatigue behavior of T91 steel in air and high oxygen concentration lead-bismuth eutectic at 450 °C. *J. Mater. Res. Technol.* **2026**, *42*, 2124–2136. [CrossRef]
5. Institute of Metal Research; Chinese Academy of Sciences. *Service Environments and Failure Modes of Structural Materials for Key Equipment in Lead-Cooled Fast Reactors*; Chinese Academy of Sciences: Beijing, China, 2024.
6. Zrodnikov, A.V.; Toshinsky, G.I.; Komlev, O.G.; Dragunov, Y.G.; Stepanov, V.S.; Klimov, N.N.; Kopytov, I.; Krushelnitsky, V. Nuclear power development in market conditions with use of multi-purpose modular fast reactors SVBR-75/100. *Nucl. Eng. Des.* **2006**, *236*, 1490–1502. [CrossRef]
7. Grasso, G.; Petrovich, C.; Mattioli, D.; Artioli, C.; Sciora, P.; Gugiu, D.; Bandini, G.; Bubelis, E.; Mikityuk, K. The core design of ALFRED, a demonstrator for the European lead-cooled reactors. *Nucl. Eng. Des.* **2014**, *278*, 287–301. [CrossRef]
8. OECD/NEA. Handbook on lead-bismuth eutectic alloy and lead properties, materials compatibility, thermalhydraulics and technologies. In *Nuclear Science*; OECD, Nuclear Energy Agency: Paris, France, 2015.
9. Gong, X.; Short, M.P.; Auger, T.; Charalampopoulou, E.; Lambrinou, K. Environmental degradation of structural materials in liquid lead- and lead-bismuth eutectic-cooled reactors. *Prog. Mater. Sci.* **2022**, *126*, 100920. [CrossRef]
10. Martinelli, L.; Balbaud-Célérier, F.; Terlain, A.; Delpech, S.; Santarini, G.; Favergeon, J.; Moulin, G.; Tabarant, M.; Picard, G. Oxidation mechanism of a Fe–9Cr–1Mo steel by liquid Pb–Bi eutectic alloy (Part I). *Corros. Sci.* **2008**, *50*, 2523–2536. [CrossRef]
11. Martinelli, L.; Balbaud-Célérier, F.; Terlain, A.; Bosonnet, S.; Picard, G.; Santarini, G. Oxidation mechanism of an Fe–9Cr–1Mo steel by liquid Pb–Bi eutectic alloy at 470 °C (Part II). *Corros. Sci.* **2008**, *50*, 2537–2548. [CrossRef]
12. Martinelli, L.; Balbaud-Célérier, F.; Picard, G.; Santarini, G. Oxidation mechanism of a Fe-9Cr-1Mo steel by liquid Pb–Bi eutectic alloy (Part III). *Corros. Sci.* **2008**, *50*, 2549–2559. [CrossRef]
13. Martinelli, L.; Balbaud-Célérier, F. Modelling of the oxide scale formation on Fe-Cr steel during exposure in liquid lead-bismuth eutectic in the 450–600 °C temperature range. *Mater. Corros.* **2011**, *62*, 531–542. [CrossRef]
14. Zhou, Z.; Du, J.; Tian, C.; Peng, X.; Wu, Y.; Lv, X.; Zhang, Y.; Chen, Z. Local mechanical properties of corrosion layers formed on T91 and SS316L steels after exposure to static liquid LBE at 500 °C for 1000 h obtained by nano-indentation. *Nucl. Eng. Technol.* **2024**, *56*, 3067–3075. [CrossRef]
15. Wang, H.; Xiao, J.; Chai, L.; Shen, Z.; Yin, X.; Zhao, K.; Guo, N.; Yu, B.; Zeng, X.; Qiu, S. Insights into the corrosion mechanism of a 12Cr F/M steel in oxygen-saturated liquid LBE. *Corros. Sci.* **2023**, *225*, 111602. [CrossRef]
16. Zhao, Y.; Ding, S.; Du, Y.; Yang, K.; Liu, S. Effect of long-term thermal aging on lead-bismuth eutectic corrosion behavior of 9Cr ferritic/martensitic steel. *J. Mater. Sci. Technol.* **2025**, *210*, 299–311. [CrossRef]
17. Hai, C.; Huang, T.; Cui, H.; Huang, Q.; Zhai, Y. Insight into the corrosion mechanism of pre-stressed 9Cr RAFM steel with long-term thermal aging exposed to oxygen saturated LBE at 550 °C. *Corros. Sci.* **2026**, *261*, 113619. [CrossRef]
18. Zhang, H.; Wang, H.; Xiong, S.; Han, H.; Volz, S.; Ni, Y. Multiscale modeling of heat dissipation in 2D transistors based on phosphorene and silicene. *J. Phys. Chem. C* **2018**, *122*, 2641–2647. [CrossRef]
19. Zhang, L.-Z.; Zeng, S.; Zhou, J. A molecular level performance manipulation of thermal conductivity and moisture diffusivity through a composite membrane considering interfacial resistance. *J. Membr. Sci.* **2019**, *583*, 231–247. [CrossRef]
20. Beygelzimer, E.; Beygelzimer, Y. Thermal conductivity of oxide scale and its components in the range from 0 °C to 1300 °C: Generalized estimates with account for movability of phase transitions. *arXiv* **2021**, arXiv:2110.11632. [CrossRef]
21. Li, M.; Akoshima, M.; Endo, R.; Ueda, M.; Tanei, H.; Susa, M. Thermal diffusivity and conductivity of Fe_3O_4 scale provided by oxidation of iron. *ISIJ Int.* **2022**, *62*, 275–277. [CrossRef]
22. Slack, G.A. Thermal conductivity of MgO, Al_2O_3, $MgAl_2O_4$, and Fe_3O_4 crystals from 3° to 300°K. *Phys. Rev.* **1962**, *126*, 427–441. [CrossRef]

23. Liu, Y.; Xing, J.; Li, Y.; Tan, J.; Sun, L.; Yan, J. Mechanical properties and anisotropy of thermal conductivity of $Fe_{3-x}Cr_xO_4$ (x = 0–3). *J. Mater. Res.* **2016**, *31*, 3805–3813. [CrossRef]
24. Blumm, J. The Laser Flash Technique: A Widespread Technology for Measurement of the Thermal Diffusivity of Solids and Liquids. *Int. J. Thermophys.* **2025**, *46*, 39. [CrossRef]

Disclaimer/Publisher's Note: The statements, opinions and data contained in all publications are solely those of the individual author(s) and contributor(s) and not of MDPI and/or the editor(s). MDPI and/or the editor(s) disclaim responsibility for any injury to people or property resulting from any ideas, methods, instructions or products referred to in the content.